# Sensing Organic Molecules by Charge Transfer through Aptamer-Target Complexes: Theory and Simulation

Maria Schill and Thorsten Koslowski*

Institut für Physikalische Chemie, Universität Freiburg, Albertstrasse 23a, D-79104 Freiburg im Breisgau, Germany

ABSTRACT: Aptamers, i.e., short sequences of RNA and single-stranded DNA, are capable of specificilly binding objects ranging from small molecules over proteins to entire cells. Here, we focus on the structure, stability, dynamics, and electronic properties of oligonucleotides that interact with aromatic or heterocyclic targets. Large-scale molecular dynamics simulations indicate that aromatic rings such as dyes, metabolites, or alkaloides form stable adducts with their oligonucleotide host molecules at least on the simulation time scale. From molecular dynamics snapshots, the energy parameters relevant to Marcus' theory of charge transfer are computed using a modified Su–Schrieffer–Heeger Hamiltonian, permitting an estimate of the charge transfer rates. In many cases, aptamer binding seriously influences the charge transfer kinetics and the charge carrier mobility within the complex, with conductivities up to the nanoampere range for a single complex. We discuss the conductivity properties with reference to potential applications as biosensors.
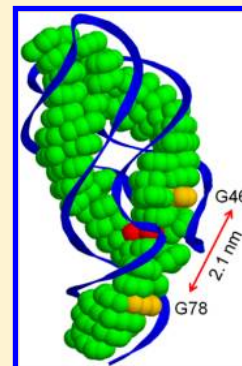
1. INTRODUCTION

Aptamers are short sequences of single-stranded RNA- and DNA-macromolecules with 20 to 100 base pairs that fold into a well-defined three-dimensional structure. Due to their great structural diversity they can recognize a broad spectrum of different target molecules and bind them with high affinity and specificity.[1–3]

Aptamers are common in nature. They act as small noncoding RNA molecules and riboswitches, which are fundamental to the regulation of gene expression by metabolite recognition.[4–7] For example, riboswitches act as genetic regulatory elements within untranslated regions of bacterial mRNA. They can respond to intracellular concentrations of specific metabolites (i.e., their target molecules) and regulate the expression of genes which play a crucial role in the metabolism and transport of these targets. Riboswitches consist of an aptamer part which is essential for the detection of the target and a regulatory domain referred to as the expression modulator. Within a family of riboswitches, the sequence and structure are conserved, with the exception of the region binding the target. In this work, we focus on 14 purine riboswitches and mutants from *B. subtilis* and four preQ$_1$ riboswiches from *B. subtilis* and *T. tengcongensis* which recognize different target molecules.

Synthetic aptamers are designed using an in vitro selection process called SELEX (systematic evolution of ligands by exponential enrichment),[8,9] to create host systems for targets like nucleosides, nucleotides and nucleobases,[10–13] protein cofactors,[14–16] amino acids,[17–19] carbohydrates,[20,21] alcaloides,[22] organic dyes,[23–25] antibiotics,[26–28] proteins,[29,30] inorganic ions,[31] or even entire cells.[32] As examples studied in this work, we have the malachite green aptamer that recognizes the respective organic dye and *N,N′*-tetramethyl-rosamine, the Diels–Alder aptamer which catalyzes the enantioselective carbon–carbon bond formation of a diene and a dienophile, or the HCV IRES domain in IIa single-stranded RNA from the hepatitis C virus which specifically binds to a potent small-molecule inhibitor of HCV replication. The riboswitches and synthetic aptamers studied in this work are depicted in Figure 1, incorporating a typical target molecule.

Aptamers are promising candidates for biosensors.[33–37] Compared to antibodies, they have the advantage of a comparatively simple synthesis using PCR techniques, they are less prone to irreversible thermal denaturation, and they are less problematic concerning modifications like the addition of a fluorophore or quencher. Many biosensors work as a switchable electron transfer system that changes its charge transfer properties via conformational changes before or after target binding. Usually, the presence of a target influences the distance between the electrode and a charge donor and induces a current that can be detected at a macroscopic level.[38–42]

Oligonucleotide fragments can act as molecular conductors: excess positive charges can migrate along DNA double strands on length scales as large as 170 Å (or 50 base pairs) via hopping or superexchange processes.[43] Furthermore, nanoscopic setups containing DNA fragments show conductivities in the 10 nA range upon the application of an external potential of 1 V.[44] Motivated by recent experimental and theoretical progress in understanding these phenomena,[45–47] we apply atomistic simulations and electronic structure calculations to one of the key elements of aptamer-based biosensors, the so-called recognition component. In this way, we are able to address the question of the stability of aptamer–target complexes and their electronic conductivity, a property with the potential of
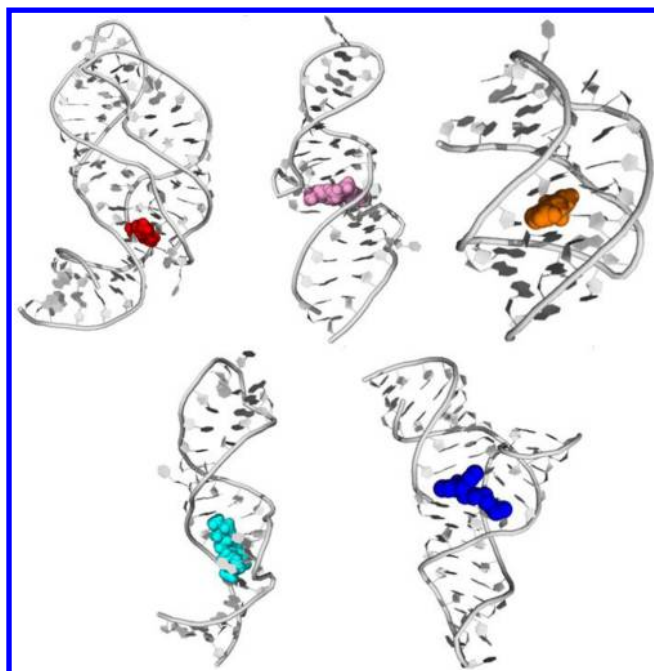
Figure 1. Cartoon models of aptamers, ribozymes and riboswitches studied in this work. From left to right, top to bottom: guanine riboswitch (protein database identification 1Y27[52]), malachite green aptamer (1Q8N[55]), preQ$_1$ riboswitch (3Q50[60]), HCV IRES domain within the IIa single-stranded RNA from the hepatitis C virus (2KTZ[57]), and a Diels−Alder ribozyme (1YKV[58]). RNA backbones are shown as strands, nucleobases as filled polygons, and target molecule atoms as spheres.

directly generating or supporting a macroscopically detectable signal.

The remaining part of this work is organized as follows. In the next chapter, we describe the molecular dynamics simulations used to create sample geometries, the electronic structure model and its use within Marcus' theory of charge transfer. Results are presented and discussed in the third section, with a guanine-recognizing purine riboswitch as an example discussed in detail, including an error analysis. Additional numerical results are given for other purine riboswitches, preQ$_1$ riboswitches, and various synthetic aptamers, e.g., the malachite green and the Diels−Alder aptamer. Conclusions are drawn in the final section.

2. MODEL AND METHODS

2.1. System Setup and Molecular Dynamics. The systems used in this work are based on structures determined by X-ray crystallography and NMR spectroscopy: the models for bacterial mRNA purine riboswitches with different targets like guanine, adenine, or xanthine are taken from the work of Daldrop et al.[48] (protein database codes 2XO1, 2XNZ, 2XO0, and 2XNW), Gilbert et al.[49−51] (3G4M, 3GAO, 3GER, 3GES, and 2G9C), Serganov et al.[52] (1Y27 and 1Y26), Batey et al.[53] (1U8D), and Dixon et al.[54] (3LA5). Sequence lengths range from 65 to 68 bases, and the sequence lengths are also listed in Table 2.

The synthetic malachite green aptamer models with two different targets are taken from Flinders et al.[55] (1Q8N) and Baugh et al.[56] (1F1T). The synthetic HCV IRES domain aptamer from Hepatitis C IIa RNA with two isomer drug targets has been characterized by Paulsen et al.[57] (2KTZ and

2KU0). For the synthetic Diels−Alder aptamer we take structures from the work of Serganov et al.[58] (1YKV). Finally, for the models for bacterial mRNA preQ$_1$ riboswitches with two different targets we use the X-ray crystal structures solved by Spitale et al.[59] (3GCA), Jenkins et al.[60] (3Q50), and Klein et al.[61] (3FU2) and solution NMR data by Kang et al.[62] (2L1V).

All molecular dynamics simulations were performed using the *sander* routine of version 12 of the AMBER molecular modeling suite.[63] The RNA fragments have been described by the parmbsc0 force field.[64] The aptamers have been embedded in a TIP3P water box.[65] The parameters for all target molecules were taken from the gaff force field,[66] missing parameters were generated using the *antechamber* and *tleap* routines of the AMBER molecular modeling program package.[63] Geometries have been optimized on the density functional theory level using the B3LYP functional and a 6-31G** basis set, partial charges have been obtained by an electrostatic potential fit to a single-point Hartree−Fock electronic structure calculation, following the standard procedure of the Amber package. The ab initio calculations were performed with the help of the *Gaussian 09* program package.[67]

For each simulation, the following parameters have been used: a total duration of 10 ns, the SHAKE algorithm was applied to constrain bond lengths involving hydrogens, and a 10 Å cutoff radius for short-range interactions. The particle-mesh Ewald method was used for the computation of the electrostatic potential. The temperature was controlled by a Langevin thermostat with a collision frequency of 2 ps^{-1}, whereas the pressure was controlled with a Berendsen-type scaling scheme with a 1 ps coupling constant. As the output of our molecular dynamics simulations, we generated 500 structural snapshots serving as the geometrical basis of the electronic structure calculations described below. These snapshots have been selected as follows: after an equilibration period of 1.4 ns, a snapshot was taken every 2 ps, ensuring a statistical independence of the electronic couplings computed from these geometries.

2.2. Electronic Structure Model. The description of the electronic structure of the aptamers and their host molecules follows the work of Cramer et al.[70] It is based on an approximate $\sigma-\pi$ separation. For the systems under review, the highest molecular orbitals show a π character; they may become centers of localization for excess holes, the dominant charge carrier species in DNA charge transfer. Electron holes in low-energy orbitals such as those of the RNA backbone are not involved in direct charge transfer.

The electronic structure theory is based upon a chemically specific Su−Schrieffer−Heeger Hamiltonian, which has been carefully parametrized using ab initio calculations.[47] It consists of a one-electron tight-binding part, a harmonic interaction between the nuclei, and a linear electron−phonon coupling term and reads

$$\hat{H}_{TB} = \sum_i \varepsilon_i a_i^\dagger a_i + \sum_{ij} \nu_{ij} a_i^\dagger a_j \tag{1}$$

$$\hat{H}_N + \hat{H}_I = \sum_{ij} \left[\frac{k}{2}(x_i - x_j)^2 + \alpha(x_i - x_j)(a_i^\dagger a_j + a_i a_j^\dagger) \right] \tag{2}$$

$$\hat{H}_{SSH} = \hat{H}_{TB} + \hat{H}_N + \hat{H}_I \tag{3}$$

The ε_i denote the valence orbital ionization potentials of the atoms, the ν_{ij} are the tight-binding coupling matrix elements, and $a_i^\dagger a_j$ are the operators for the creation and annihilation of electrons within a set of $2p_z$ and $3p_z$ basis atomic orbitals. The basis is assumed to be orthogonal. The x_i represent nuclear coordinates, α is the electron−phonon coupling parameter of the SSH model, and k is the force constant of a chemical bond between nearest neighbors. For each molecule, a set of π atomic orbitals is constructed as being orthogonal to the plane of the molecule.

The SSH Hamiltonian $\hat{H}_{SSH}$ can be separated into an electronic and a classical nuclear component by using a displaced phonon coordinate.[71] In the restricted Hartree−Fock (HF) mean field approximation, we obtain the transformed Hamiltonian

$$\hat{H}_{SSH} = \sum_i \varepsilon_i a_i^\dagger a_i + \sum_{ij} (\nu_{ij} - 4U_{SSH}\bar{n}_{ij})a_i^\dagger a_j$$
$$+ 4U_{SSH}\sum_{ij}\bar{n}_{ij}^2 \tag{4}$$

The tight-binding bond order $\bar{n}_{ij}$ is proportional to the deviation of the distance between neighboring atoms from a single bond $x_i - x_j$. Originally, the SSH model was designed to describe the electronic structure of doped polyacetylene.[72]

This Hamiltonian is supplemented by an outer-sphere contribution, which describes the interaction of a polarized dielectric continuum with the excess charge residing in the π orbital system. We follow Marcus' description of polarization phenomena[73] via an ensemble of charges $e\Delta z_i$ centered within spheres of diameter σ_i, which are embedded in a uniform dielectric medium. The corresponding outer sphere reorganization energy reads

$$\lambda_{out} = \frac{e^2}{4\pi\varepsilon_0}\left(\frac{1}{\varepsilon_\infty} - \frac{1}{\varepsilon_s}\right)\left(\sum_i \frac{\Delta z_i^2}{\sigma_i} - \sum_{i<j} \frac{\Delta z_i \Delta z_j}{r_{ij}}\right) \tag{5}$$

Here, ε_∞ and ε_s are the high-frequency and static limits of the dielectric permittivity, $\varepsilon(\omega)$, respectively. Neglecting long-range interactions, this energy can be interpreted as a local electron−electron attraction term within a spin-free Hubbard Hamiltonian, as described in refs 74−76. It is given by

$$\hat{H}_{OUT} = -U_{ee}\sum_i (n_i - \bar{n}_{i,0})^2 \tag{6}$$

The attractive part of the Hamiltonian can be interpreted as a nonretarded reaction field with a strength U_{ee}. In this manner, the SSH model is extended by coupling it to a polarizable environment. Applying a Hartree-like mean-field approximation to the combined Hamiltonian, we find[71]

$$\hat{H} = \sum_i \varepsilon_i a_i^\dagger a_i + \sum_{ij} \nu_{ij} a_i^\dagger a_j - 4U_{SSH}\sum_{ij} \bar{n}_{ij} a_i^\dagger a_j$$
$$- 2U_{ee}\sum_i n_i(\bar{n}_i - \bar{n}_{i,0}) \tag{7}$$

The overbars indicate the computation of expectation values, in this case from the previous step of a self-consistent field procedure. We refer to this Hamiltonian as the extended Su−Schrieffer−Heeger model.

3. RESULTS AND DISCUSSION

3.1. Parametrization. To obtain the extended SSH model parameters of the π orbital subsystem of the aptamers and the target molecules, we follow ref.[70] Ab initio calculations have been performed at the DFT level (vacuum, B3LYP functional and 6-31G** basis set, *Gaussian 09* program package[67]) in order to obtain the energies of the occupied molecular orbitals, ε_{DFT}. The extended SSH model intramolecular parameters have been varied within a Monte Carlo procedure until the difference of the empirical orbital energies, ε_{SSH}, to the ab initio references became a minimum (ref 68, p. 46, Figure 3.8). For the off-diagonal Hubbard parameter we have retained a value of $U_{SSH} = 0.313$ eV. This set of parameters has been checked by inspecting those molecular orbitals which are potential centers of hole localization, the HOMOs (ref 68, p. 48, Figure 3.9). The thus obtained diagonal tight-binding parameters of the extended SSH Hamiltonian are listed in Table 1.

Table 1. Diagonal Tight-Binding Parameters of the Extended SSH Hamiltonian, eq 7[a]

atom	ε/eV
C	0.0
CH$_3$	−6.926
N sp^2	−1.502
N sp^3	−4.504
O keto	−2.254
O hydroxy	−6.021
Cl	−5.460

[a]The ε_C value is taken as the zero of energy.

Intermolecular couplings have been fitted to the splitting of the HOMOs of two stacked nucleobases. For numerical reasons, only a parallel arrangement of the nucleobases ensures a proper determination of the matrix elements. We find $V_{ppm} = V_{ppm}^0 \exp(-\alpha r)$ $(m = \sigma,\pi)$ with $V_{pp\sigma}^0 = 43.2$ eV, $V_{pp\pi}^0 = -11.6$ eV and $\alpha = 1.45$ Å^{-1} (ref 68, p. 49, Figure 3.10). These resulting nearest neighbor GG couplings (stacked: ~200 meV, twisted: ~50 meV) are slightly less than those obtained by Voityuk et al.[69] (stacked: 430 meV, twisted: 84 meV).

The off-diagonal elements between two p_z orbitals which are neighbors have the same value $\nu_0 = -2.873$ eV for all bases, and just as the diagonal elements they are independent of the bases. In addition, the ionization energies from the DFT calculations were used to adjust total diagonal shifts for all ε_i of a given base. The ionization potentials are identified as the energies of the highest occupied molecular orbitals of DFT quantum chemical calculations in the vacuum, all SSH energies are corrected individually to meet the DFT values.

3.2. Charge Transfer through a Riboswitch As an Example. In this section, we discuss charge transfer through the wild type guanine riboswitch of *B. subtilis* in the absence and in the presence of guanine (**1**) as a target molecule. A cartoon model of the X-ray structure[52] (1Y27) is shown in Figure 2.

To compute the electronic structure, 500 snapshots have been taken from a simulation of 10 ns. During that simulation, the guanine guest molecule did not leave its binding pocket. Depending on the initial conditions, an excess hole charge may localize on each of the guanines, the nucleobases with the highest ionization potential in solution. Each converged
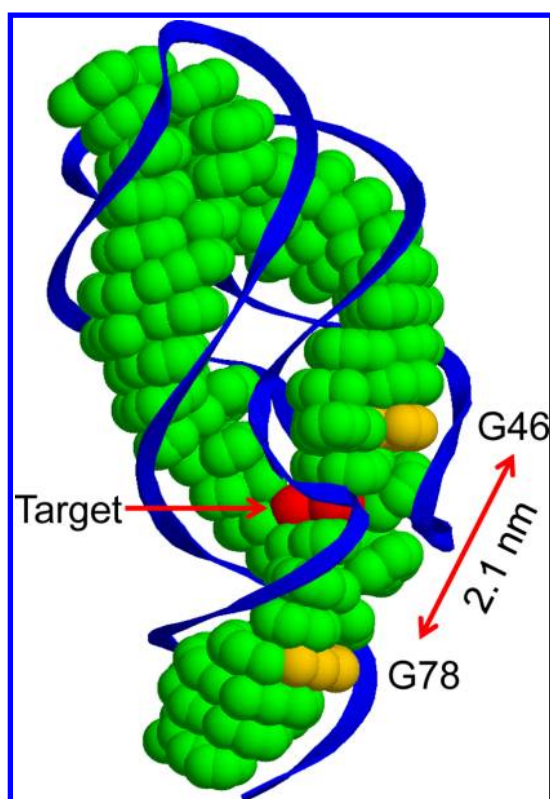
Figure 2. Cartoon model of the wild type guanine riboswitch in the presence of the guanine target. The aptamer guanine bases are plotted in green, and the other aptamer bases are gray. We indicate the gap between guanine G46 and G78 which plays a crucial role in charge transfer through the system.

solution of the Hamiltonian 7 is characterized by a distinct charge and bond order distribution or, in terms of quantum chemistry, its density matrix. For two solutions, one can interpolate between the density matrices, leading to a plot shown in Figure 3. It resembles the standard representation of
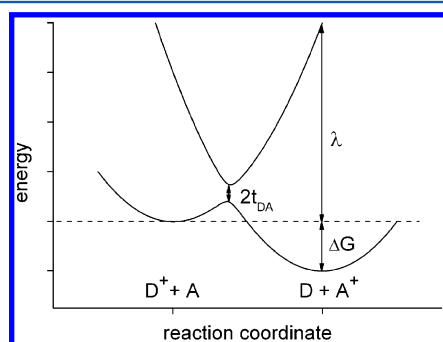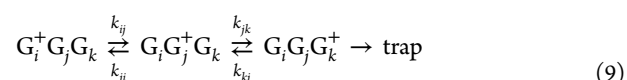

Figure 3. Free energy as a function of the reaction coordinate for the charge transfer between a donor and acceptor system with different free energy minima. Example for charge transfer between a guanine as donor and a target like PQ0‡ as acceptor. The reorganization energy λ and the effective tunnel splitting $2t_{DA}$ are shown.

Marcus' theory of charge transfer: two parabola that are split at the point of their intersection. From this figure, the energies relevant to Marcus' theory can be read directly: the reorganization energy λ, the thermodynamic driving force ΔG, and the electronic tunnel splitting t_{DA}. As an alternative to using λ and ΔG, it is possible to make use of the left and the

right activation barrier, E_A. For small couplings, the charge transfer rates between two guanines i and j can be estimated as

$$k_{ij} = \frac{t_{DA}^2}{\hbar} \sqrt{\frac{\pi}{\lambda k_B T}} \exp\left(-\frac{(\lambda + \Delta G)^2}{4\lambda k_B T}\right) \tag{8}$$

For guanine–guanine self-exchange in a symmetric environment, we have the special case $\Delta G = 0$. As a result of the extended SSH model, we get the information which bases and targets act as centers of charge localization, and we can calculate the transfer rates k_{ij} between the base- or target-positions i and j for the forward and the backward reaction. During the dynamic simulation the charge transfer rates k_{ij} between the single steps fluctuate because of the different mutual orientation of the two fragments under review. Consequently, we take the arithmetic average of 500 k_{ij} for each charge transfer step. To get the overall charge transfer rate k_S through the entire system, we set up a kinetic scheme based on reactions of the type

$$G_i^+ G_j G_k \underset{k_{ji}}{\overset{k_{ij}}{\rightleftharpoons}} G_i G_j^+ G_k \underset{k_{kj}}{\overset{k_{jk}}{\rightleftharpoons}} G_i G_j G_k^+ \rightarrow \text{trap} \tag{9}$$

where G_i, G_j, and G_k are centers of charge localization.

For each system, only the fastest charge transfer path is considered. The corresponding first-order kinetic equations for the populations c_i read

$$\frac{dc_i}{dt} = \sum_j k_{ij} c_j - c_i \sum_l k_{il} \tag{10}$$

Using the ansatz

$$\vec{c_i}(t) = \vec{c_i}^{\,0} \exp(-\lambda t) \tag{11}$$

we obtain the eigenvalue problem

$$(\mathbf{K} - \lambda \mathbf{1}) \vec{c}^{\,0} = \vec{0} \tag{12}$$

Its eigenvalues and eigenvectors give the general solution of the system of first-order differential equations

$$\vec{c}(t) = \sum_\alpha A_\alpha \vec{c_\alpha}^{\,0} \exp(-\lambda_\alpha t) \tag{13}$$

$\mathbf{K}$ the tridiagonal matrix of reaction coefficients k_{ij}. The coefficients A_α are computed to match the initial conditions, $\vec{c_i}(t = 0) = \delta_{1,i}$, i.e., localization on the first guanine in the sequence of nucleobases within the aptamer.

For the guanine riboswitch, the charge transfer path follows the guanines 42, 27, 46, 90, 78, and 79, where 90 constitutes the target molecule. For the decadic logarithms of the electronic couplings, $\log(2t_{DA})$, along this sequence, we obtain 1.24 ± 0.50 ($D = G_{42}$, $A = G_{27}$), -0.82 ± 0.56 ($D = G_{27}$, $A = G_{46}$), -0.21 ± 0.52 ($D = G_{46}$, $A = G_{90}$), 1.46 ± 0.49 ($D = G_{90}$, $A = G_{78}$), and -1.31 ± 0.43 ($D = G_{78}$, $A = G_{79}$). Thus, typical errors in t amount to half an order of magnitude, leading to an error in k_S of 1 order of magnitude.

In figure 4 we show the population of the trap, c_{trap}, as a function of the decadic logarithm of time. As a trap, we consider a hypothetical object connected to the final base of the aptamer via a fast irreversible reaction. We define a characteristic time $t_{1/2}$ at which half of the trap is populated, and define $k_S = 1/t_{1/2}$. For the aptamer–target complex, we also show the influence of sampling upon the final kinetics of the system. We obtain $k_S = 2.7 \times 10^5$ s^{-1} for 100 realizations, 3.2×10^5 s^{-1} for
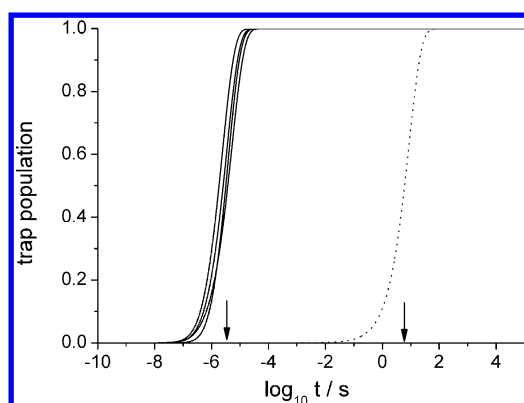
Figure 4. Net kinetics of charge transfer in the guanine riboswitch 1Y27: trap population as a function of the logarithm of time. Solid lines: presence of the target molecule for 1000, 2000, 500, and 100 snapshots (top of the curves, from left to right). Dotted line: absence of the target molecule, the arrows indicate the characteristic time scale, $t_{1/2}$.

500 realizations, 5.3×10^5 s^{-1} for 1000 realizations, and 4.0×10^5 s^{-1} for 2000 realizations.

For guanine−guanine (G-G) hopping, we have self-exchange, $\Delta G = 0$. Using $U_{ee} = 0.8$ eV,[70] we obtain 0.42 eV for the reorganization energy λ,[78] corresponding to an activation barrier E_A of 0.11 eV. This value may be too small, in particular in comparison to recent computer simulations on DNA[79] and proteins,[80] which suggest values in excess of 1 eV. Furthermore, ab initio inner sphere reorganization energies alone amount to 0.48 eV (U) to 0.92 eV (T), whereas the corresponding SSH model energies range from 0.06 eV (C) to 0.15 eV (A). We note that the ab initio calculations also include C−H and N−H bond stretching contributions, which would qualify as outer sphere contributions within the SSH model, which only takes deformations within the π subsystem into account. Nevertheless, the total λ should always exceed the smallest ab initio inner sphere contribution to this quantity. As a consequence, we have performed all calculations with an additional value of λ = 0.9 eV. As will transpire below, the numerical values of the net charge transfer rates do at most decrease by a factor of 3.

We compute average transfer rates k_S of 0.17 s^{-1} in the absence and 3.2×10^5 s^{-1} in the presence of an intercalating guanine target. This notable difference of 6 orders of magnitude in the charge transfer rates can be rationalized as follows. In the absence of the target, hopping between G46 and G78 constitutes a kinetic bottleneck, with an interguanine distance of 2.1 nm. This distance is roughly halfed once the target is introduced, with a t_{DA} that essentially depends exponentially on the donor−acceptor distance, $t_{DA} \approx \exp(-\beta r_{DA})$ with $\beta \simeq 0.55$ Å^{-1}.[81] Although two hops have to be performed in the presence of the target to bridge the gap, the overall reaction becomes significantly faster, as each of the steps takes place on a much faster time scale than the single step in the absence of the target.

3.3. Charge transfer through riboswitches: hopping vs superexchange. Guanine and adenine riboswitches and mutants thereof are able to host a broad spectrum of target molecules with different affinities, characterized by the corresponding dissociation constant, K_D, as listed in Table 2. The target molecules studied here are shown in Figures 5 and 6. The molecules shown in Figure 5 can act as centers of localization and carry an excess hole. For the molecules

Table 2. System Overview and Computed Net Charge Transfer Rates[a]

T	A	n_B	PDB	$-pK_D$ (nM)	$\tilde{k}_{S,42}$ (s^{-1})	$k_{S,42}$ (s^{-1})	$\tilde{k}_{S,90}$ (s^{-1})	$k_{S,90}$ (s^{-1})
2‡	GUA	65	2B57*	1.2[50]	6.6×10^{-2}	6.5×10^3	4.0×10^{-2}	3.0×10^3
1‡	GUA	68	1Y27	0.7[77]	0.17	3.2×10^5	8.0×10^{-2}	1.8×10^5
3‡	GUA	67	3GAO	4.6[49]	0.19	3.2×10^3	9.4×10^{-2}	1.4×10^3
4‡	GUA	68	1U8D	2.9[53]	2.3	2.9×10^2	1.3	94
5‡	GUA	67	2XNW*	5.6[48]	6.6×10^{-2}	14	4.0×10^{-2}	11
6	ADE	71	3LA5*	3.0[54]	7.1×10^{-2}	0.20	4.6×10^{-2}	0.12
7	GUA	67	2XNZ*	5.0[48]	4.6×10^{-2}	0.47	2.4×10^{-2}	0.31
8	GUA	67	2XO0*	4.9[48]	7.1×10^{-2}	0.45	4.6×10^{-2}	0.28
9	GUA	67	2G9C*	3.3[51]	2.2×10^{-2}	0.25	1.5×10^{-2}	0.18
10	ADE	71	1Y26	2.5[48]	2.9×10^{-2}	0.11	2.0×10^{-2}	7.0×10^{-2}
11	GUA	67	2XO1*		7.1×10^{-2}	17	4.6×10^{-2}	16
12	GUA	67	3G4M	3.6[49]	0.71	3.8	0.25	1.9
13	GUA	67	3GES*	3.3[49]	0.25	0.24	0.16	0.16
14	GUA	67	3GER	2.9[49]	2.8	0.63	2.1	0.42
15	MGR	38	1Q8N	2.9[55]	3.3×10^4	2.9×10^8	2.5×10^4	2.1×10^8
16	MGR	38	1F1T	1.6[56]	3.3×10^4	1.5×10^8	2.5×10^4	1.1×10^8
17‡	preQ₁	33	3GCA*		4.2×10^6	2.1×10^9	3.1×10^6	1.4×10^9
18‡	preQ₁	33	3Q50*		4.3×10^6	1.3×10^{10}	3.1×10^6	8.1×10^9
18‡	preQ₁	33	3FU2*	1.3[61]	2.5×10^8	2.3×10^9	1.8×10^8	1.4×10^9
18‡	preQ₁	36	2L1V*		8.3×10^7	1.1×10^9	5.8×10^7	3.9×10^8
19‡	HCV	38	2KTZ	4.0[57]	6.0×10^4	1.8×10^9	4.1×10^4	1.0×10^9
20‡	HCV	38	2KU0	3.4[57]	6.0×10^4	5.0×10^8	4.1×10^4	1.7×10^8
21	DA	49	1YKV	3.0[58]	2.2×10^7	4.4×10^6	1.5×10^7	2.9×10^6

[a]Target T, aptamer A, number of bases n_B, protein data base identifier, decadic logarithm of the aptamer-target dissociation constant K_D, overall charge transfer rate in the absence of targets, $\tilde{k}_{S,42}$ and overall charge transfer rate in the presence of targets, $k_{S,42}$ for λ = 0.42 eV, overall charge transfer rate in the absence of targets, $\tilde{k}_{S,90}$ and overall charge transfer rate in the presence of targets, $k_{S,90}$ for λ = 0.90 eV. The double dagger symbol (‡) labels the targets which can act as centers of charge localization, and the asterisk (*) indicates mutants.
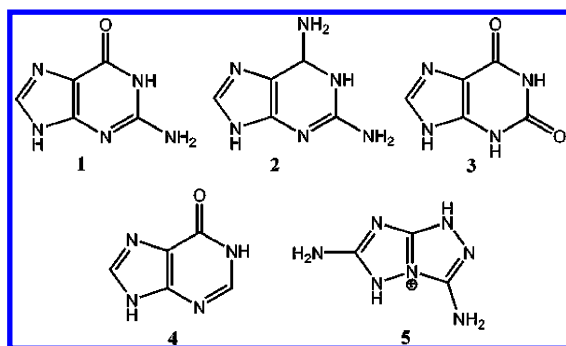
Figure 5. Structure of purine riboswitch target molecules that act as centers of localization for excess positive charges, as indicated by the double dagger symbol, ‡. **1** GUA‡, guanine; **2** 6AP‡, 2,6-diaminopurine; **3** XAN‡, xanthine; **4** HPA‡, hypoxanthine; **5** ZZR‡, 3,6-diamino-1,5-dihydro[1,2,4]triazolo[4,3-b][1,2,4]triazol-4-ium.
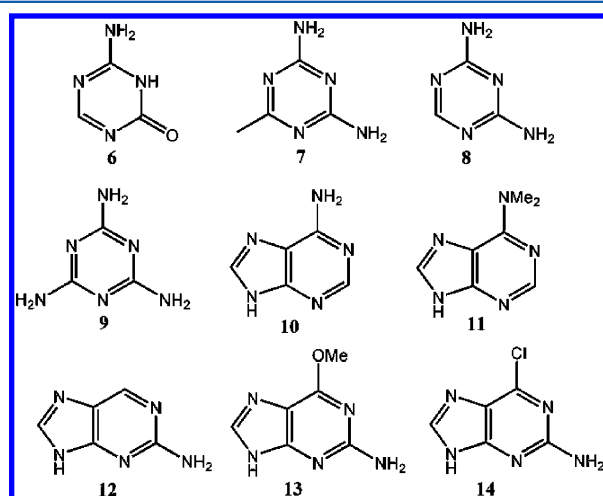
Figure 6. Structure of purine riboswitch target molecules that participate in charge transfer via superexchange: **6** 5AZ, 6-amino-1,3,5-triazin-2(1H)-one; **7** 3AW, 6-methyl-1,3,5-triazine-2,4-diamine; **8** ZZS, 1,3,5-triazine-2,4-diamine; **9** 3AY, pyrimidine-2,4,6-triamine; **10** ADE, adenine; **11** N6M, N-methyl-9H-purin-6-amine; **12** 2BP, 9H-purin-2-amine; **13** 6GO, 6-O-methylguanine; **14** 6GU, 6-chloroguanine.

presented in Figure 6, the attempt to localize a charge initially using a target molecule cation within the self-consistent solution to eq 7 failed. Instead, the positive charge always drifted toward a nearby guanine. The systems under review here are also listed in Table 2, with computed charge transfer rates and experimental dissociation constants. Of the 14 riboswitch−ligand complexes studied here, five permit an excess charge localization on the target molecule. They are labeled by a double dagger symbol, e.g. HPA‡. In the case of charge localization on an intermediate, the overall charge transfer rate always increases considerably once a target molecule is complexed by the riboswitch.

If charge localization on the target molecule fails, overall reaction rates will be slightly enhanced or will be unaffected (cf. Table 2). Superexchange alone does not seem to be sufficiently efficient to overcome the kinetic bottleneck, which is due to the large spatial gap between two guanines, e.g., G46 and G78 in 1Y27.

We note that the only targets studied here which allow a localization of a positive charge are purine bases such as GUA‡ (**1**), 6AP‡ (**2**), XAN‡ (**3**), and HPA‡ (**4**), with the exception

of the triazole ZZR‡ (**5**), whereas there is no localization on triazine bases 5AZ (**6**), 3AW (**7**) and ZZS (**8**), a pyridine base 3AY (**9**) and purine bases like ADE (**10**), N6M (**11**), 2BP (**12**), 6GO (**13**), and 6GU (**14**). Inspecting the Lewis structures, we gain the impression that two fused heterocyclic rings and three sp^3 hybridized nitrogens are required to induce hole localization. In the case of hole localization on the target molecules, the overall rate always increases, with enhancement factors ranging from two to 10^6. In the presence of the guest molecule, reaction rates k_S range from 14 to 3.2×10^5 s^{-1}.

For charge transfer within oligonucleotides, an additional process has to be considered. For large interguanine distances (more than four base pairs $\simeq 14$ Å), intermediate localization on adenines may occur, a mechanism that is usually referred to as adenine−adenine hopping. Here, the dependence of the net charge transfer rates on the interguanine distances follows a power law. Applying the parameters used here, rates for B-DNA as an ordered, stacked system at most amount to 10^4 s^{-1}. Any rate indicating the capture of a target should be higher than this limit in order to obtain a signal.

Failing charge localization on the target molecule, the overall rates k_S are rather small, they range from 0.47 to 17 s^{-1} in the presence of a guest molecule. Again, charge transfer rates always increase upon the introduction of a target molecule.

3.4. Malachite Green Recognition. In the past, malachite green has been used as a fungizide, especially in fish farming. Now considered as toxic and potentially cancerogeneous, its use has been banned in many countries. In the EU, the maximum allowable concentration in food has been set to 0 μg/kg, requiring particularly sensitive analytical techniques.

The malachite green aptamer (1Q8N and 1F1T) and its target molecules are shown in Figure 7. Apart from hosting the malachite green molecule MGR (**15**), it can also accommodate N,N'-tetramethyl-rosamine (ROS, **16**) with an even higher affinity, cf. Table 2.

The malachite green aptamer consists of 38 bases from which 13 are the charge-trapping guanines. The two organic dye targets already carry a positive charge which is delocalized over their π-systems, which makes them unlikely centers of excess hole localization. This is consistent with our calculations, where the two dyes did not act in this manner. Nevertheless, the overall charge transfer rate increases from 3.4×10^4 to 2.9×10^8 s^{-1} for MGR and to 1.5×10^8 s^{-1} for ROS. Thus, rates change by a factor of 10 thousand upon the introduction of a guest molecule.

Charge transfer between guanines, G8 and G29, can be identified as the kinetic bottleneck within the system, they exhibit an edge-to-edge distance of 8.0 Å. Here, the two dyes participate in the charge transfer process as via a superexchange mechanism with a remarkable efficiency.

3.5. Charge Transfer through the preQ$_1$ Riboswitch. We have investigated the synthetic preQ$_1$ riboswitch with three different sequences and two different targets called PQ0‡ (**17**) and PRF‡ (**18**) (see Figure 7).

The preQ$_1$ rioboswitches stem from B. subtilis (wildtype (3FU2) and mutant (2L1V)) and T. tengcongensis (3GCA and 3Q50) with 33 or 36 bases, respectively. Of these, 6 or 7 are guanines that may act as centers of excess charge localization. In addition, the metabolites **17** and **18** also act as temporary hole traps.

Charge transfer in this aptamer-riboswitch complex is very fast. The calculated charge transfer rate k_S amounts to 2.1×10^9s^{-1} for the PQ0‡ ligand and ranges from 1.1×10^9 to $1.3 \times$
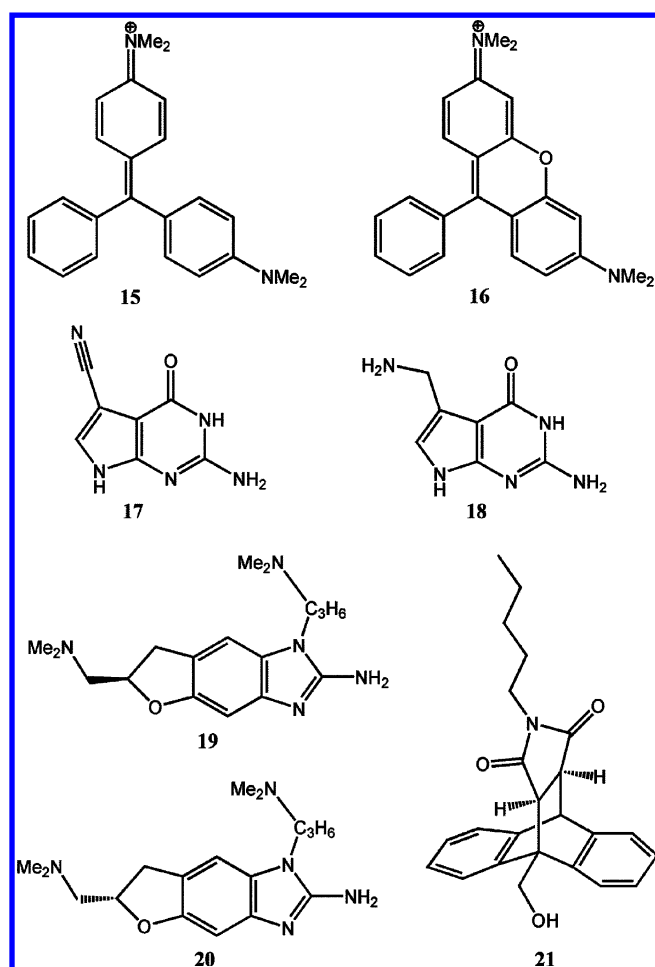
Figure 7. Structure of the target molecules interacting with the malachite green aptamer, the synthetic HCV IRES, the preQ₁ riboswitch, the aptamer domain of Hepatitis C IIa RNA and the Diels−Alder ribozyme (the double dagger symbol, ‡, marks centers of excess positive charge localization): **15** MGR, malachite green; **16** ROS, N,N'-tetramethyl-rosamine; **17** PQ0‡ or preQ₀, 7-deaza-7-aminomethyl-guanine; **18** PRF‡ or preQ₁, 2-amino-4-oxo-4,7-dihydro-3H-pyrrolo[2,3-D]pyrimidine-5-carbonitrile; **19** ISH‡, (7R)-7-[(dimethylamino)methyl]-1-[3-(dimethylamino)-propyl]-7,8-dihydro-1H-furo[3,2-e]benzimidazol-2-amine; **20** ISI‡, (7S)-7-[(dimethylamino)methyl]-1-[3-(dimethylamino)-propyl]-7,8-dihydro-1H-furo[3,2-e]benzimidazol-2-amine; and **21** DAI, (3AS,9AS)-2-pentyl-4-hydroxymethyl-3A,4,9,9A-tetrahydro-4,9[1′,2′]-benzeno-1H-benz[F]isoindole-1,3(2H)-dione.

10^{10} s^{-1} for PRF‡ (see Table 2). For the *B. subtilis* system, this is about 10^3 to 10^4 faster compared to rates obtained in the absence of the ligand. For *T. tengcongensis*, the corresponding enhancement is of the order of 10^1 to 10^2.

3GCA and 3Q50 have an identical sequence of bases, yet the overall charge transfer rate through the corresponding aptamer-riboswitch complex differs by a factor of 6, with a potential of distinguishing two target molecules using the same riboswitch.

3.6. Charge Transfer through Virus mRNA. We describe charge transfer through the synthetic HCV IRES domain aptamer from hepatitis C virus IIa mRNA. It consists of 38 bases of which 11 guanines with the potential of localizing hole charges. Its target molecules, ISH‡ (**19**) and ISI‡ (**20**), are potent small-molecule inhibitors of HCV replication.[57]

In this systems the overall charge transfer rate is enhanced considerably as compared to the ligand-free systems, as the

drug molecules can also act as potential centers of charge localization. Hence, we find direct hopping between the guanine and the target as a mechanism rather than super-exchange. For the aptamer-target complex we have calculated a charge transfer rate $k_S = 1.8 \times 10^9$ s^{-1} with ISH‡ (**19**) as a target and 5.0×10^8 s^{-1} with ISI‡ (**20**) as a target (see Table 2). This amounts to an enhancement factor of 10^4 to 10^5 in comparison to the ligand-free aptamer.

3.7. Charge Transfer through a Synthetic Diels−Alder Ribozyme. We now turn to the synthetic Diels−Alder ribozyme, where the reaction product of the enzymatically catalyzed, selective and enantiopure 4 + 2-cycloaddition, DAI (**21**) (Figure 7), also serves as a target molecule with a moderate K_D.

This ribozyme consists of 49 bases, of which 18 are guanines that may host excess positive charges. In notable contrast to the systems discussed above, the presence of the ligand slows down the charge transfer reaction considerably. We find a charge transfer rate k_S of 4.4×10^6 s^{-1} in the presence of the Diels−Alder reaction product and 2.2×10^7 s^{-1} in its absence (see Table 2). Although DAI (**21**) has the potential to act as a superexchange partner for charge transfer between the guanines G2 and G4, the bottleneck for hole transfer, it has a net negative impact on the charge transfer properties due to the induction of an unfavorable change of the ribozyme structure: the G2−G4 distance increases from ∼7 Å in the absence to ∼10 Å in the presence of the reaction product.

4. CONCLUSIONS

In this work, we have investigated the charge transfer properties of ribozymes, riboswitches and synthetic aptamers in the presence and in the absence of target molecules. System geometries have been generated using molecular dynamics simulations. Throughout the simulation time scale of 10 to 20 ns, the complexes turned out to be stable. Simulation snapshots have been taken as input of empirical electronic structure computations with an extended, chemically specific Su-Schrieffer-Heeger Hamiltonian as the underlying model. Via an interpolation scheme, the energy parameters relevant to Marcus' theory of charge transfer have been computed, permitting an estimate of the corresponding rates.

For all systems studied here, a pronounced difference in the overall charge transfer rate was observed once the target molecule had been accommodated. We attribute this effect to the structure of the binding pocket, which is usually poor in RNA guanine, the centers of excess hole localization. Bridging the large gap between two guanines around the pocket via hopping constitutes the kinetic bottleneck of the system. Once a target molecule is introduced, this gap may be bridged by an additional center of localization or a superexchange partner. Of these classes of molecules, those participating in hopping, such as **1−5** and **17−20**, turned out to be more efficient in enhancing the overall charge transfer rate than those participating in superexchange.

To observe a signal generated caused by the presence of a target molecule, the following requirements have to be fulfilled:

(i) at least one of the overall charge transfer rates has to be larger than 10^4 s^{-1} in order to distinguish the signal from a background generated by adenine−adenine hopping, as discussed in section 3.3.

(ii) the difference in the overall rates in the absence ($\tilde{k}_S$) and in the presence (k_S) of the target molecule has to be

large. Fluctuations in the local rates k_{ij} amount to at most 1–2 orders of magnitude, suggesting a ratio of $k_S/\tilde{k}_S$ of the same order

(iii) host and guest molecule have to show a high affinity, i.e., a small dissociation constant K_D.

Inspecting Table 2, we note that for the guanine riboswitches, these conditions can only be met by 1Y27 as a host molecule and guanine as a target, all other systems have overall rates smaller than 10^4 s^{-1}. Unfortunately, even fulfilling all the conditions listed above may not be sufficient to distinguish two target molecules: the isomer **19** binds less effective to the HCV IRES domain than **20**, which is overcompensated by an overall charge transfer rate through the aptamer-target complex including **20**, which is roughly three times faster.

We predict an excellent performance of the preQ$_1$ riboswitches that bind to the targets **17** and **18**: the overall charge transfer rates in the presence of target molecules are high ($k_S > 10^9$ s^{-1}), and k_S and $\tilde{k}_S$ show a sufficient difference. Only for one of the systems, K_D is known and measured as small. For the preQ$_1$ riboswitch–PRF complex (PDB ID 3Q50), we observe the highest rate of all systems studied here, $k_S = 1.3 \times 10^{10}$ s^{-1}. With an elementary charge of 1.6×10^{-19} C, we find an electric current of 2 nA, which is in the range of detection within a nanoscopic setup Thus, combining suitable pairs of aptamers and target molecules may even permit the detection of single molecules.

A cartoon model of a possible macroscopic realization is presented in Figure 8: A light-sensitive complex C, e.g., of the
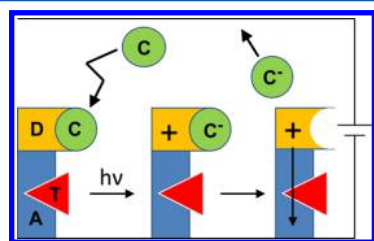
Figure 8. Cartoon model of a possible realization of an aptamer-based sensor. Aptamer A, target molecule T, complex C, and complex-binding DNA fragment D. For details, see text.

ruthenium polypyridyl type, binds to a DNA fragment D. Upon red light irradiation, positive and negative charges are separated, with the positive charge traveling through the aptamer–target AT complex bridging D and the cathode of an electrochemical setup. To balance the charge flow, C$^-$ diffuses to the anode. In the absence of the target molecule, conductivity through the aptamer decreases, and the photochemically induced charges recombine prior to inducing a current. Nanoscopic realizations of aptamer-based sensors would resemble setups presented by Porath et al.[44] or Barton and co-workers[82]

Whereas the predictions made in this work still await an experimental verification or falsification, we note that the underlying concepts have turned out to be successful in other contexts, e.g., the description of DNA conductivity.[70] We are confident that the methods used here may not only help to describe charge transfer processes in existing aptamer–target complexes but may also allow the design of aptamers particularly suitable to both specifically binding the target and supporting a high current.

■ AUTHOR INFORMATION

Corresponding Author
*E-mail: Thorsten.Koslowski@physchem.uni-freiburg.de.

■ REFERENCES

(1) Gold, L.; Polisky, B.; Uhlenbeck, O.; Yarus, M. *Annu. Rev. Biochem.* **1995**, *64*, 763–797.
(2) Wilson, D. S.; Szostak, J. W. *Annu. Rev. Biochem.* **1999**, *68*, 611–647.
(3) Klussmann, S. *The Aptamer Handbook: Functional Oligonucleotides and Their Applications*; Wiley-VCH: Weinheim, Germany, 2006.
(4) Nudler, E.; Mironov, A. S. *Trends Biochem. Sci.* **2004**, *29*, 11–17.
(5) Nudler, E. *Cell* **2006**, *1*, 19–22.
(6) Breaker, R. R. *Mol. Cell* **2011**, *43*, 867–879.
(7) Bastet, L.; Dube, A.; Masse, E.; Lafontaine, D. A. *Mol. Microbiol.* **2005**, *80*, 1148–1154.
(8) Joyce, G. F. *Angew. Chem.* **2007**, *119*, 6540–6557.
(9) Tuerk, C.; Gold, L. *Science* **1990**, *249*, 505–510.
(10) Sassanfar, M.; Szostak, J. W. *Nature* **1993**, *364*, 550–553.
(11) Burke, D. H.; Gold, L. *Nucleic Acids Res.* **1997**, *25*, 2020–2024.
(12) Connell, G. J.; Yarus, M. *Science* **1994**, *264*, 1137–1141.
(13) Kiga, D.; Futamura, Y.; Sakamoto, K.; Yokoyama, S. *Nucleic Acids Res.* **1998**, *26*, 1755–1760.
(14) Lorsch, J. R.; Szostak, J. W. *Biochemistry* **1994**, *33*, 973–982.
(15) Lauhon, C. T.; Szostak, J. W. *J. Am. Chem. Soc.* **1995**, *117*, 1246–57.
(16) Burgstaller, P.; Famulok, M. *Angew. Chem.* **1994**, *33*, 1084–1087.
(17) Famulok, M.; Szostak, J. W. *J. Am. Chem. Soc.* **1992**, *114*, 3990–3991.
(18) Connell, G. J.; Illangesekare, M.; Yarus, M. *Biochemistry* **1993**, *32*, 5497–5502.
(19) Majerfeld, I.; Yarus, M. *Nat. Struct. Biol.* **1994**, *1*, 287–292.
(20) Yang, Q.; Goldstein, I. J.; Mei, H.; Engelke, D. R. *Proc. Natl. Acad. Sci. U.S.A.* **1998**, *95*, 5462–5467.
(21) Srisawat, C.; Goldstein, I. J.; Engelke, D. R. *Nucleic Acids Res.* **2001**, *29* (No.2), e4.
(22) Win, M. N.; Klein, J. S.; Smolke, C. D. *Nucleic Acids Res.* **2006**, *34*, 5670–5682.
(23) Ellington, A. D.; Szostak, J. W. *Nature* **1990**, *346*, 818–822.
(24) Ellington, A. D.; Szostak, J. W. *Nature* **1992**, *355*, 850–852.
(25) Grate, D.; Wilson, C. *Proc. Natl. Acad. Sci. U.S.A.* **1999**, *96*, 6131–6136.
(26) Lato, S. M.; Boles, A. R.; Ellington, A. D. *Chem. Biol.* **1995**, *2*, 291–303.
(27) Burke, D. H.; Hoffman, D. C.; Brown, A.; Hansen, M.; Pardi, A.; Gold, L. *Chem. Biol.* **1997**, *4*, 833–843.
(28) Wallace, S. T.; Schroeder, R. *RNA* **1998**, *4*, 112–123.
(29) Ruckman, J.; Green, L. S.; Beeson, J.; Waugh, S.; Gillette, W. L.; Henninger, D. D.; Claesson-Welsh, L.; Janji, N. *J. Biol. Chem.* **1998**, *273*, 20556–20567.
(30) Yamamoto, R.; Katahira, M.; Nishikawa, S.; Baba, T.; Taira, K.; Kumar, P. K. *Genes Cells* **2000**, *5*, 371–388.
(31) Zivarts, M.; Liu, Y.; Breaker, R. R. *Nucleic Acids Res.* **2005**, *33*, 622–631.
(32) Chen, N.; Zhang, Z.; Soontornworajit, B.; Zhou, J.; Wang, Y. *Biomaterials* **2012**, *33*, 1353–1362.
(33) Song, S.; Wang, L.; Li, J.; Zhao, J.; Fan, C. *Trends Anal. Chem.* **2008**, *27*, 108–117.
(34) Mok, W.; Li, Y. *Sensors* **2008**, *8*, 7050–7084.
(35) Radi, A. E. *Int. J. Electrochem.* **2011**, 1–17.

(36) Han, K.; Liang, Z.; Zhou, J. N. *Sensors* **2010**, *10*, 4541–4557.

(37) Strehlitz, B.; Nikolaus, N.; Stoltenburg, R. *Sensors* **2008**, *8*, 4296–4307.

(38) Xiao, Y.; Lubin, A. A.; Heeger, A. J.; Plaxco, K. W. *Angew. Chem.* **2005**, *44*, 5456–5459.

(39) Pividori, M. I.; Merkoci, A.; Alegret, S. *Biosens. Bioelectron.* **2000**, *15*, 291–303.

(40) Radi, A. E.; Sanchez, J. L. A.; Baldrich, E.; O'Sullivan, C. K. *Anal. Chem.* **2005**, *77*, 6320–6323.

(41) Zhang, X.; Zhao, Z.; Mei, H.; Qiao, Y.; Liu, Q.; Xia, T.; Luo, W.; Fang, X. *Analyst* **2011**, *136*, 4764–4769.

(42) Genereux, J. C.; Boal, A. K.; Barton, J. K. *J. Am. Chem. Soc.* **2010**, *132*, 891–905.

(43) Nunez, M. E.; Noyes, K. T.; Barton, J. K. *Chem. Biol.* **2002**, *9*, 403–415.

(44) Porath, D.; Bezryadin, A.; de Vries, S.; Dekker, C. *Nature* **2000**, *430*, 635–638.

(45) Warshel, A. *Acc. Chem. Res.* **2002**, *35*, 385–395.

(46) Mallajosyula, S. S.; Lin, J. C.; Cox, D. L.; Pati, S. K.; Singh, R. R. P. *Phys. Rev. Lett.* **2008**, *101*, 176805ff.

(47) Cramer, T.; Krapf, S.; Koslowski, T. *J. Phys. Chem. C* **2007**, *111*, 8105–8110.

(48) Daldrop, P.; Reyes, F. E.; Robinson, D. A.; Hammond, C. M.; Lilley, D. M.; Batey, R. T.; Brenk, R. *Chem. Biol.* **2011**, *18*, 324–335.

(49) Gilbert, S. D.; Reyes, F. E.; Edwards, A. L.; Batey, R. T. *Adaptive Struct.* **2009**, *17*, 857–868.

(50) Gilbert, S. D.; Stoddard, C. D.; Wise, S. J.; Batey, R. T. *J. Mol. Biol.* **2006**, *359*, 754–768.

(51) Gilbert, S. D.; Mediatore, S. J.; Batey, R. T. *J. Am. Chem. Soc.* **2006**, *128*, 14214–14215.

(52) Serganov, A.; Yuan, Y. R.; Pikovskaya, O.; Polonskaia, A.; Malinina, L.; Phan, A. T.; Hobartner, C.; Micura, R.; Breaker, R. R.; Patel, D. *J. Chem. Biol.* **2004**, *11*, 1729–1741.

(53) Batey, R. T.; Gilbert, S. D.; Montange, R. K. *Nature* **2004**, *432*, 411–415.

(54) Dixon, N.; Duncan, J. N.; Geerlings, T.; Dunstan, M. S.; McCarthy, J. E. G.; Leys, D.; Micklefield, J. *Proc. Natl. Acad. Sci. U.S.A.* **2010**, *107*, 2830–2835.

(55) Flinders, J.; DeFina, S. C.; Brackett, D. M.; Baugh, C.; Wilson, C.; Dieckmann, T. *ChemBioChem* **2004**, *5*, 62–72.

(56) Baugh, C.; Grate, D.; Wilson, C. *J. Mol. Biol.* **2000**, *301*, 117–128.

(57) Paulsen, R. B.; Seth, P. P.; Swayze, E. E.; Griffey, R. H.; Skalicky, J. J.; Cheatham, T. E.; Davis, D. R. *Proc. Natl. Acad. Sci. U.S.A.* **2010**, *107*, 7263–7268.

(58) Serganov, A.; Keiper, S.; Malinina, L.; Tereshko, V.; Skripkin, E.; Höbartner, C.; Polonskaia, A.; Phan, A. T.; Wombacher, R.; Micura, R.; Dauter, Z.; Jäschke, A.; Patel, D. *J. Nat. Struct. Biol.* **2005**, *12*, 218–224.

(59) Spitale, R. C.; Torelli, A. T.; Krucinska, J.; Bandarian, V.; Wedekind, J. E. *J. Biol. Chem.* **2009**, *28*, 11012–11016.

(60) Jenkins, J. L.; Krucinska, J.; McCarty, R. M.; Bandarian, V.; Wedekind, J. E. *J. Biol. Chem.* **2011**, *286*, 24626–24637.

(61) Klein, D. J.; Edwards, T. E.; Ferré-D'Amaré, A. R. *Nat. Struct. Mol. Biol.* **2009**, *16*, 343–344.

(62) Kang, M.; Peterson, R.; Feigon, J. *Mol. Cell* **2010**, *39*, 653–655.

(63) Case, D. A.; Darden, T. A.; Cheatham, T. E.; Simmerling, C. L.; Wang, J.; Duke, R. E.; Luo, R.; Walker, R. C.; Zhang, W.; Merz, K. M.; et al. *Amber 12*. Technical report, University of California: San Francisco, 2012.

(64) Perez, A.; Marchan, I.; Svozil, D.; Sponer, J.; Cheatham, T. E.; Laughton, C. A.; Orozco, M. *Biophys. J.* **2007**, *92*, 3817–3829.

(65) Jorgensen, W. L.; Chandrasekhar, J.; Madura, J. D.; Impey, R. W.; Klein, M. L. *J. Chem. Phys.* **1983**, *79*, 926–935.

(66) Wang, J.; Wolf, R. M.; Caldwell, J. W.; Kollman, P. A.; Case, D. A. *J. Comput. Chem.* **2004**, *25*, 1157–1174.

(67) Frisch, M. J.; et al. *Gaussian 09*, revision A.1; Gaussian Inc.: Wallingford, CT, 2009.

(68) Cramer, T.; *Ladungstransfer in DNA: Ein atomistisches Modell*, Ph.D. Dissertation, University of Freiburg, 2006. Available online as http://www.freidok.uni-freiburg.de/volltexte/2592/

(69) Voityuk, A. A.; Rösch, N.; Bixon, M.; Jortner, J. *J. Phys. Chem. B* **2000**, *104*, 9740–9745.

(70) Cramer, T.; Krapf, S.; Koslowski, T. *J. Phys. Chem. B* **2004**, *108*, 11812–11819.

(71) Rateitzak, M.; Koslowski, T. *Chem. Phys. Lett.* **2003**, *377*, 455–461.

(72) Su, W. P.; Schrieffer, J. R.; Heeger, A. J. *Phys. Rev. B* **1980**, *22*, 2099–2111.

(73) Marcus, R. A. *J. Chem. Phys.* **1956**, *24*, 966–978.

(74) Hubbard, J. *Proc. R. Soc. A* **1963**, *276*, 238–257.

(75) Georges, A.; Kotliar, G.; Krauth, W.; Rozenberg, M. J. *Rev. Mod. Phys.* **1996**, *68*, 13–125.

(76) Utz, N.; Koslowski, T. *Chem. Phys.* **2002**, *282*, 389–397.

(77) Mandal, M.; Breaker, R. R. *Nat. Rev.* **2004**, *5*, 451–463.

(78) Fukuzumi, S.; Nishimine, M.; Ohkubo, K.; Tkachenko, N. V.; Lemmetyinen, H. *J. Phys. Chem. B* **2003**, *107*, 12511–12518.

(79) Steinbrecher, T.; Koslowski, T.; Case, D. A. *J. Phys. Chem. B* **2008**, *112*, 16935–16944.

(80) Krapf, S.; Weber, S.; Koslowski, T. *Phys. Chem. Chem. Phys.* **2012**, *14*, 11518–11524.

(81) Giese, B.; Biland, A. *Angew. Chem., Int. Ed. Engl.* **2000**, *39*, 3490–3491.

(82) Wang, H.; Muren, N. B.; Ordinario, D.; Gorodetsky, A. A.; Barton, J. K. *Chem. Sci.* **2012**, *3*, 62–65.